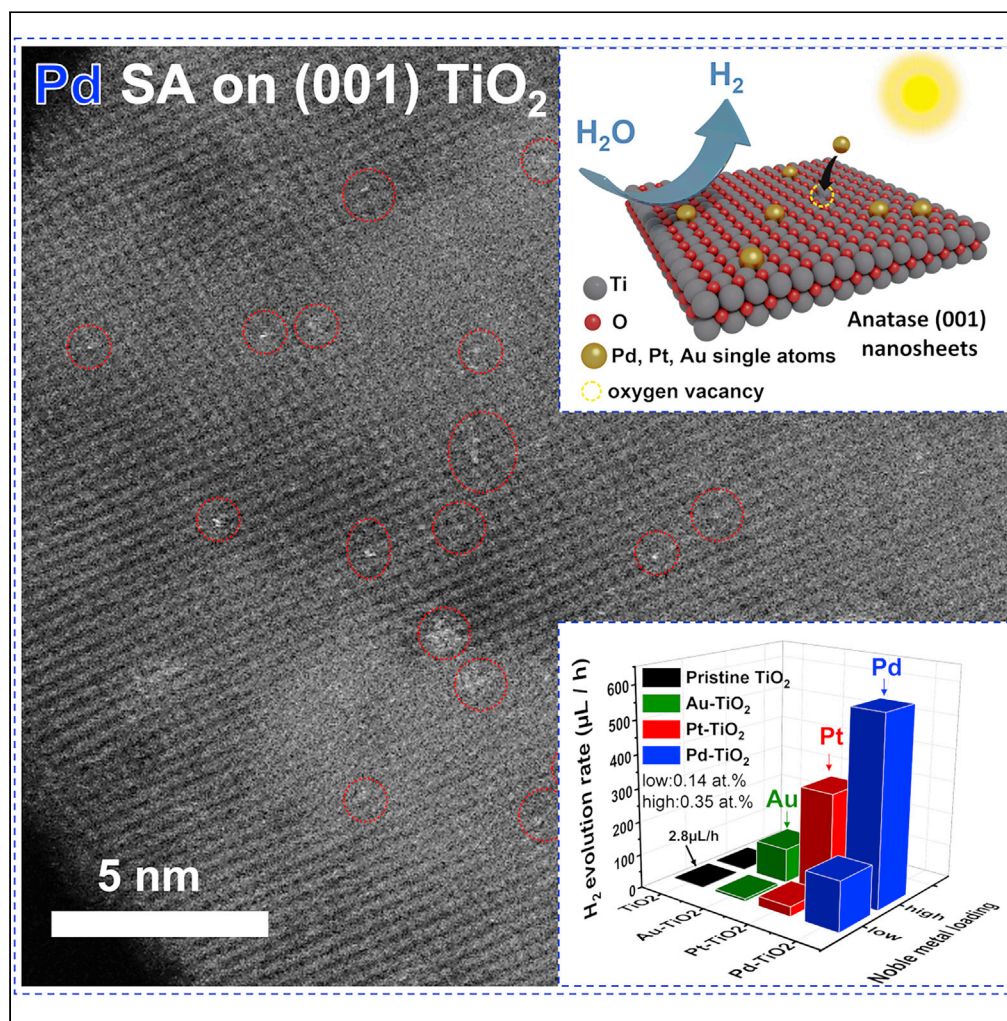**Article**

As a single atom Pd outperforms Pt as the most active co-catalyst for photocatalytic H₂ evolution

Gihoon Cha,
Imgon Hwang,
Seyedsina Hejazi,
..., Natalia V.
Skorodumova,
Erdmann
Spiecker, Patrik
Schmuki

schmuki@ww.uni-erlangen.de

Highlights

Pd, Pt, or Au single atoms decorated {001} anatase TiO_2 nanosheets

Controlled surface trapping of SA by surface vacancies (Ti^{3+}-O_v, reducing treatment)

Photocatalytic H_2 evolution rates result in the HER sequence Pd > Pt > Au for SAs

The higher activity of Pd than Pt can be ascribed to charge localization on the SAs

Article

As a single atom Pd outperforms Pt as the most active co-catalyst for photocatalytic H$_2$ evolution

Gihoon Cha,[1] Imgon Hwang,[1] Seyedsina Hejazi,[1,8] Ana S. Dobrota,[2] Igor A. Pašti,[2,3] Benedict Osuagwu,[1] Hyesung Kim,[1] Johannes Will,[4] Tadahiro Yokosawa,[4] Zdeněk Badura,[5] Štěpán Kment,[5] Shiva Mohajernia,[1,8] Anca Mazare,[1] Natalia V. Skorodumova,[3,6] Erdmann Spiecker,[4] and Patrik Schmuki[1,5,7,9,*]

SUMMARY

Here, we evaluate three different noble metal co-catalysts (Pd, Pt, and Au) that are present as single atoms (SAs) on the classic benchmark photocatalyst, TiO$_2$. To trap the single atoms on the surface, we introduced controlled surface vacancies (Ti^{3+}-O$_v$) on anatase TiO$_2$ nanosheets by a thermal reduction treatment. After anchoring identical loadings of single atoms of Pd, Pt, and Au, we measure the photocatalytic H$_2$ generation rate and compare it to the classic nanoparticle co-catalysts on the nanosheets. While nanoparticles yield the well-established the hydrogen evolution reaction activity sequence (Pt > Pd > Au), for the single atom form, Pd radically outperforms Pt and Au. Based on density functional theory (DFT), we ascribe this unusual photocatalytic co-catalyst sequence to the nature of the charge localization on the noble metal SAs embedded in the TiO$_2$ surface.

Single atom (SA) catalysts not only allow maximizing the utilization efficiency of expensive metals but also often enable unique reaction pathways and thus have become a frontline in the field of catalysis and more recently in the field of photocatalysis (Flytzani-Stephanopoulos, 2014; Fu et al., 2003; Gao et al., 2020; Gates et al., 2017; Heiz et al., 1999; Hu et al., 2021; Liu, 2017; Qiao et al., 2011; Wang et al., 2018; Yang et al., 2013; Zhu et al., 2017). A most challenging photocatalytic reaction remains the production of H$_2$ using sunlight and aqueous reactants. In such photocatalytic approaches, mobile photoelectrons are generated in a semiconductor that then react with water or protons to produce H$_2$ (Kudo and Miseki, 2009; Osterloh, 2013; Wang and Domen, 2020). In order to reach reasonable reaction rates, the hydrogen evolution reaction (HER) needs to be catalyzed—typically by various noble metals such as Pt, Pd, Rh, etc. (Nørskov et al., 2005; Parsons, 1958; Seh et al., 2017; Sheng et al., 2013; Trasatti, 1972; Wang et al., 2020; Yao et al., 2019). To select an optimized catalyst, a most common approach is to adopt principles from electrocatalysis, where a huge body of experimental and theoretical work deals with extracting the most optimal HER catalysts and giving a reasoning for the ranking of the reactivity (Nørskov et al., 2005; Parsons, 1958; Trasatti, 1972). Classic experimental volcano plots are in good agreement with theoretical concepts that attribute a maximal reaction rate to an optimized hydrogen adsorption-free energy G$_H$ (Nørskov et al., 2005; Parsons, 1958; Seh et al., 2017; Sheng et al., 2013; Trasatti, 1972), and it is widely accepted in theory and experiment that Pt is the most efficient catalyst or co-catalyst for H$_2$ evolution—this for electrocatalysis as well as for photocatalysis (Seh et al., 2017; Wang and Domen, 2020; Wenderich and Mul, 2016).

In the present work, we investigate the situation of three different noble metal co-catalysts (Pd, Pt, and Au) that are anchored as single atoms on the classic benchmark photocatalyst, TiO$_2$. Generally, the main challenge in using SA as a catalyst or co-catalyst is stabilizing and controlling the distribution of isolated reactive sites on the support material (Flytzani-Stephanopoulos, 2014; Fu et al., 2003; Gao et al., 2020; Gates et al., 2017; Heiz et al., 1999; Liu, 2017; Qiao et al., 2011; Wang et al., 2018). Typically, SA can be stabilized through pinning atoms at electronic and/or structural defects, and such crystal features or localized charge cavities are reported to provide effective traps (Fu et al., 2003; Qiao et al., 2011; Wang et al., 2018). For TiO$_2$, it has recently been shown that by a defined thermal treatment of anatase in a reductive atmosphere (Ar/H$_2$), it is possible to achieve a high level of control over the Pt SA loading (Hejazi et al., 2020). This approach to control the SA trapping, we applied here to thin TiO$_2$ anatase (001) nanosheets that were grown by an established hydrothermal synthesis (Seh et al., 2017; Wenderich and Mul, 2016), as briefly described in the experimental part.
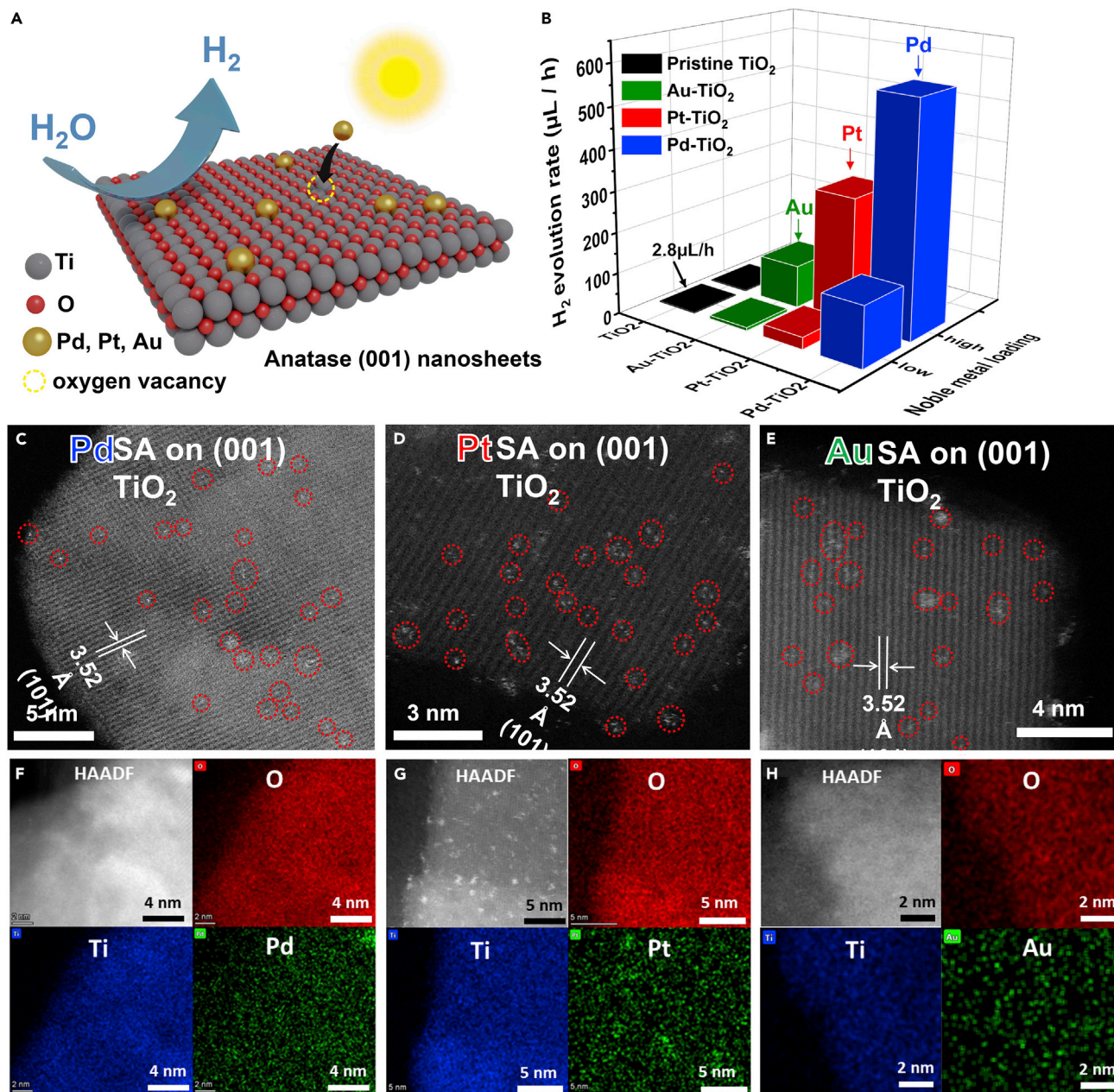
Figure 1. Photocatalytic H$_2$ evolution rate of SA noble metal-decorated TiO$_2$ nanosheets, morphology, and elemental analysis

(A) Illustration of noble metal (Pd, Pt, Au)-decorated anatase (001) TiO$_2$ nanosheets.

(B) Photocatalytic H$_2$ evolution rate of the noble metal SA-decorated TiO$_2$ nanosheets (i.e., Au-TiO$_2$, Pt-TiO$_2$, or Pd-TiO$_2$) with a low or a high (0.14 at.% and 0.35 at.%) noble metal loading;

(C–E) HAADF-STEM images of anatase (001) nanosheets with lattice fringes of 3.52 Å corresponding to anatase (101), decorated with (C) Pd SA, (D) Pt SA, and (E) Au SA.

(F–H) Corresponding EDS maps for (F) Pd, (G) Pt, and (H) Au.

These nanosheets were then reduced by a thermal Ar/H$_2$ treatment to create defined density of Ti^{3+}-O$_V$ surface traps, as outlined in Figure S1. The sheets were then immersed in dilute noble metal-containing solutions of Pd^{4+}, Pt^{4+}, and Au^{3+}, respectively. This leads to a reactive pinning of the different SA species on the nanosheet surface as illustrated in Figure 1A. We optimized this immersion treatment to achieve for the different species, with the same loadings. We established two surface concentration levels, corresponding to a loading of 0.14 at.% and 0.35 at.% as determined by X-Ray photoelectron spectroscopy

(XPS), see Table S1. These SA-loaded sheets were then investigated for their photocatalytic hydrogen evolution performance, as described in the experimental section. The results in Figure 1B show that for both SA loading levels, the H_2 evolution for the Pd-decorated TiO_2 nanosheets is considerably higher than for Pt- or Au-decorated sheets. This sequence is in stark contrast to established photocatalytic (Wang and Domen, 2020) or electrocatalytic (Trasatti, 1972; Wang and Domen, 2020) activity for crystalline Pt, Pd, or Au. For these elements in the form of crystalline nanoparticles on titania photocatalysts or when crystalline particles of these noble metals are investigated for their performances as HER electrocatalysts, almost exclusively a sequence of reactivity Pt > Pd >> Au is reported (Seh et al., 2017; Trasatti, 1972).

Figures 1C–1E show high-angle annular dark-field - scanning transmission electron microscopy (HAADF-STEM) images of the {001} surface of the TiO_2 anatase nanosheets after loading with Pd, Pt, and Au with 0.35 at.% of the noble metal. In every case, the surface is decorated with single atoms. The d spacing of the lattice fringes of 3.52 Å corresponds to anatase {101}. Scanning transmission electron microscopy-energy dispersive X-ray (STEM-EDX) mapping in Figures 1F–1H for Pd, Pt, and Au supports the notion of the noble metals being present also over a larger scale as SAs—no nanocrystalline structures can be identified. Figure S2 shows scanning electron microscopy (SEM) images of the TiO_2 nanosheets decorated with Pd, Pt, and Au for both low and high loading.

Also for the lower level of noble metal loading (0.14 at.%), HAADF-STEM images (examples are shown in Figure S3) reveal the presence of SAs. Evidently, the SAs are present at a lower surface density. Using the atom distributions from HAADF-STEM and the H_2 evolution rate, one can estimate the TOF (turnover frequency) for single atoms as described in the STAR Methods. For the two loading levels, we obtain Pd – 2.2×10^8 h^{-1}, Pt – 1.19×10^7 h^{-1}, and Au – 1.09×10^7 h^{-1} (lower loading) and Pd – 7.97×10^5 h^{-1}, Pt – 7.16×10^4 h^{-1}, and Au – 4.12×10^4 h^{-1} (higher loading). While the TOF per atom depends on the loading, the sequence of the reactivity of the SA-loaded TiO_2 remains unchanged, that is Pd > Pt > Au. It is however noteworthy that from TEM, agglomeration of SAs into multi-mers (dimers, trimers, and so on) is observed; this is particularly apparent for the higher loading (Figures 1C–1E). These different degrees of agglomeration for the two loading levels may be one reason for the different TOFs per atom for the two loading levels.

Electron paramagnetic resonance (EPR) and XPS measurements provide further details of the trapping process on the defective titania surface. Figure 2A shows EPR spectra for the plain non-reduced anatase and the nanosheets after the reduction treatment in Ar/H_2. The EPR signature after annealing in Ar/H_2 shows a response at g = 2.0 corresponding to titania-oxygen vacancies (Ti^{3+}-O_v), present in the sheets in regular lattice positions (Mohajernia et al., 2020; Naldoni et al., 2019), while the additional broad response at $g_{avg} \approx 1.93$ can be ascribed to surface-exposed Ti^{3+}-O_v states (Mohajernia et al., 2020). Evidently, this second type of defects is highly effective for SA trapping. After interaction with the dilute noble metal solutions (H_2PtCl_6, or $(NH_4)_2PdCl_6$, or $HAuCl_4 \times 3H_2O$), the nanosheet samples show a significant decrease in the magnitude of the signature at $g_{avg} \approx 1.93$ (Figure 2B). This finding strongly suggests an attachment mechanism based on a galvanic displacement reaction, where the oxidation of the Ti^{3+} state ($Ti^{3+} \rightarrow Ti^{4+}$) is coupled with the reduction of the noble metal ions, e.g., $Pt^{4+} \rightarrow Pt^{\delta+}_{surface\ trapped}$—this process eliminates EPR-active Ti^{3+} states. Based on the EPR, this reductive trapping mechanism seems to apply to all precursor salts used (i.e., H_2PtCl_6, $(NH_4)_2PdCl_6$, $HAuCl_4 \times 3H_2O$).

Moreover, also XPS after surface trapping of the different noble metal single atoms is well in line with this trapping mechanism. XPS survey spectra of the SA deposited layers are shown in Figure S4, and the corresponding high-resolution spectra are shown in Figure S5. The results show the expected presence of Ti, O, F, and the corresponding noble metal (except for some adventitious carbon). The fitted high-resolution XPS spectra for Pd3d, Pt4f, and Au4f peaks (Figures 2C–2E) further elucidate the co-ordination state and charge of the noble metals as single atoms, in the form of δ+ states coordinated to the titania surface. For the sample loaded with Pd SAs, the Pd3d peak can be fitted into four peaks (Figure 2C), where the peaks at 336.0 eV and 341.26 eV correspond to the $Pd^{\delta+}$ state ($3d_{5/2}$ and $3d_{3/2}$), while those at 337.1 eV and 342.36 eV can be attributed to the Pd^{2+} state—that is ca. 70% of the Pd would correspond to δ+ states with $\delta \approx 1.1$. For the SA Pt sample (Figure 2D), the Pt4f peak shows the presence of two different states, with $Pt^{\delta+}4f_{7/2}$ and $Pt^{\delta+}4f_{5/2}$ at 72.80 eV and 76.15 eV and $Pt^{4+}4f_{7/2}$ and $Pt^{4+}4f_{5/2}$ at 74.10 eV and 77.45 eV (80% of the Pt is in a single atom state with $\delta \approx 2$), respectively. In the case of the SA Au sample (Figure 2E), the Au4f peak can be fitted into six peaks as compared to the other evaluated SAs, a metallic state is also observed.
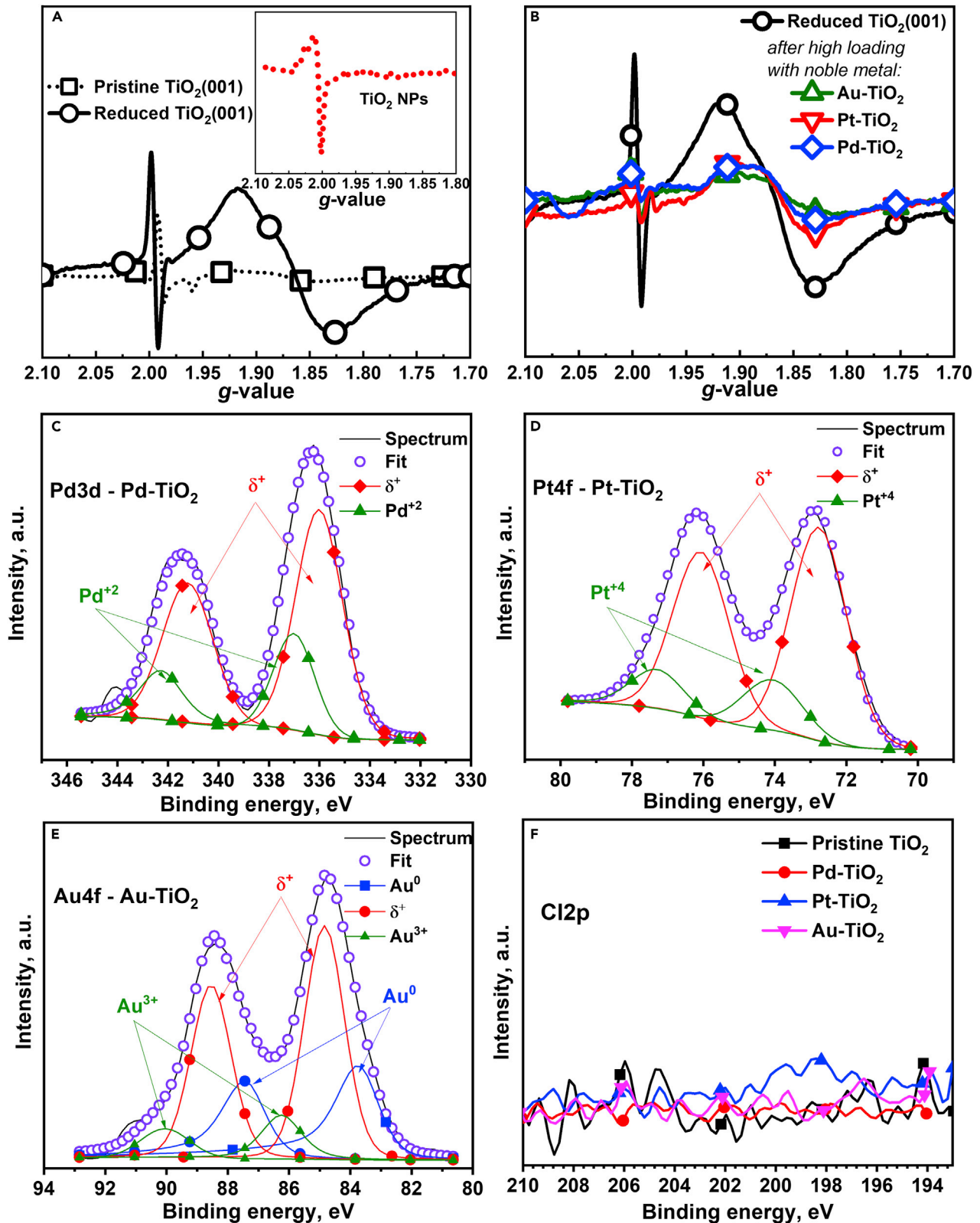
Figure 2. Structure and chemical composition of the SA noble metal-decorated TiO$_2$ nanosheets

(A and B) EPR spectra for (A) pristine and reduced TiO$_2$ nanosheets (inset: commercial TiO$_2$ anatase nanoparticles) and (B) reduced nanosheets and SA noble metal-decorated nanosheets.

(C–E) Deconvolution of the high-resolution XPS peaks showing the presence of single atom state (δ+) for the (C) Pd3d peak of the Pd-TiO$_2$, (D) Pt4f peak of the Pt-TiO$_2$, and (E) Au4f peak of the Au-TiO$_2$—all data are measured for the high loading.

(F) High-resolution XPS Cl2p peaks for pristine and noble metal SA-decorated nanosheets.

Namely, the peaks at 83.77 eV and 87.47 eV correspond to Au^{0}4f$_{7/2}$ and Au^{0}4f$_{5/2}$, the peaks at 84.84 eV and 88.54 correspond to Au$^{\delta+}$4f$_{7/2}$ and Au$^{\delta+}$4f$_{5/2}$, and, lastly, the peaks at 86.30 eV and 89.90 eV correspond to Au^{3+}4f$_{7/2}$ and Au^{3+}4f$_{5/2}$, respectively. The presence of some Au in the metallic state in the deposited sample (55% of the Au is in a SA state with δ$^{1.4+}$ and 33% is in a metallic state) can be due to the weaker interaction of Au atoms with the titanium surface (Giordano et al., 2001; Zubieta et al., 2020). It should be noted that no Cl2p peak from the precursor complex can be detected in any of the samples (Figure 2F). This indicates that the Pd, Pt, and Au signals are from fully trapped or surface-reacted noble metals, i.e., the Ti precursor in the attachment process is stripped of the original Cl$^-$ ligands.

The chemical shift for the trapped single atoms Pd, Pt, or Au (δ$^+$) originates from surface co-coordination, i.e., the metal-oxygen coordination at the surface (Daelman et al., 2019). Note that in every case δ$^+$ is lower than the precursor, and this supports the surface reaction via galvanic displacement.

The loading of the elements determined from the data in Figures 2C–2F and S6 is 0.35 at.% for Pd (1.74 wt.%), 0.35 at.% for Pt (3.00 wt.%), and 0.35 at.% for Au (3.09 wt.%)—see also Table S1. For these powders that showed a similar surface loading from XPS of ≈0.35 at.%, also chemical analysis was performed by atomic absorption spectroscopy (see experimental section). The results of 0.77 wt.% Pd, 1.19 wt.% Pt, and 1.11 wt.% Au confirm the similar loading level of the three samples. The higher absolute concentrations obtained from XPS are due to the surface sensitivity of this technique. XRD data confirmed the presence of anatase TiO$_2$ and of TiOF$_2$ in the nanosheets but could not provide any information related to the presence of the various decorated noble metal SAs (see Figure S6). The FTIR spectra are shown in Figure S7.

It is noteworthy that the sequence of the reactivity of the SA noble metal, Pd > Pt > Au, holds not only if the comparison is done for the same loading level (Figure 1B) but also if a concentration series for the noble metal salts in the precursor solution is investigated (see Figure 3A). Regardless of the precursor's concentration in the immersion solution, used for noble metal decoration, the activity of Pd-decorated TiO$_2$ nanosheets is significantly higher than that of Pt and Au in the SA form for a precursor concentration between 2.4 and 24 mM. It should be pointed out that the sequence of the reactivity is also maintained for longer illumination times (Figure 3B). To contrast these results with classic noble metal crystalline cocatalyst data, we carried out an additional set of investigations. Figure 3C gives the H$_2$ evolution activity when the TiO$_2$ nanosheets are decorated with classic Pt, Pd, and Au nanoparticles. For this, we used a chemical deposition approach described in the experimental section which leads to a loading of ≈1 wt.% for each noble metal, which are randomly dispersed on the surface of the TiO$_2$ nanosheets. SEM characterization of these nanoparticles is given in Figure S8. In every case, the nanosheets are decorated with nanoparticles of a size of ≈ 2–5 nm. Clearly, for these sized nanoparticles, the sequence of reactivity follows the classically expected sequence Pt > Pd > Au. Photocatalytic process are more complex, including light adsorption, charge separation, and catalytic reactions, and to establish a more detailed evaluation of the differences between single atom and nanoparticles supported on the TiO$_2$ nanosheets, additional investigations are needed.

In order to elucidate the unprecedented activity of the single atom Pd in comparison to SA Pt and SA Au for photocatalytic H$_2$ evolution on TiO$_2$ nanosheets, density functional theory (DFT) modeling was done. The obtained results show that incorporating the metal SAs into the O$_v$ site is energetically unfavorable to the build-up of the pure metallic phase as metal adsorption energies are below cohesive energies of all three studied metals. The interaction is the weakest in the case of Au (E_{ads}(Au) = −2.04 eV), supporting the observation of the crystalline gold too. However, O$_v$ sites do serve as binding sites at low SA concentrations. Following the general paradigm, we investigated hydrogen interaction with the SA sites, expecting that the overall trend follows volcano-type behavior. However, such behavior is not seen. In fact, E_{ads}(H) follows the trend of the observed photocatalytic activity with Pd binding H with −3.46 eV, Pt with −3.22 eV, and Au with only −2.04 eV. With the addition of the second H to the SA sites, the situation gets even more complicated, as this trend gets lost. However, if mobile photoelectrons are generated, they should go to the
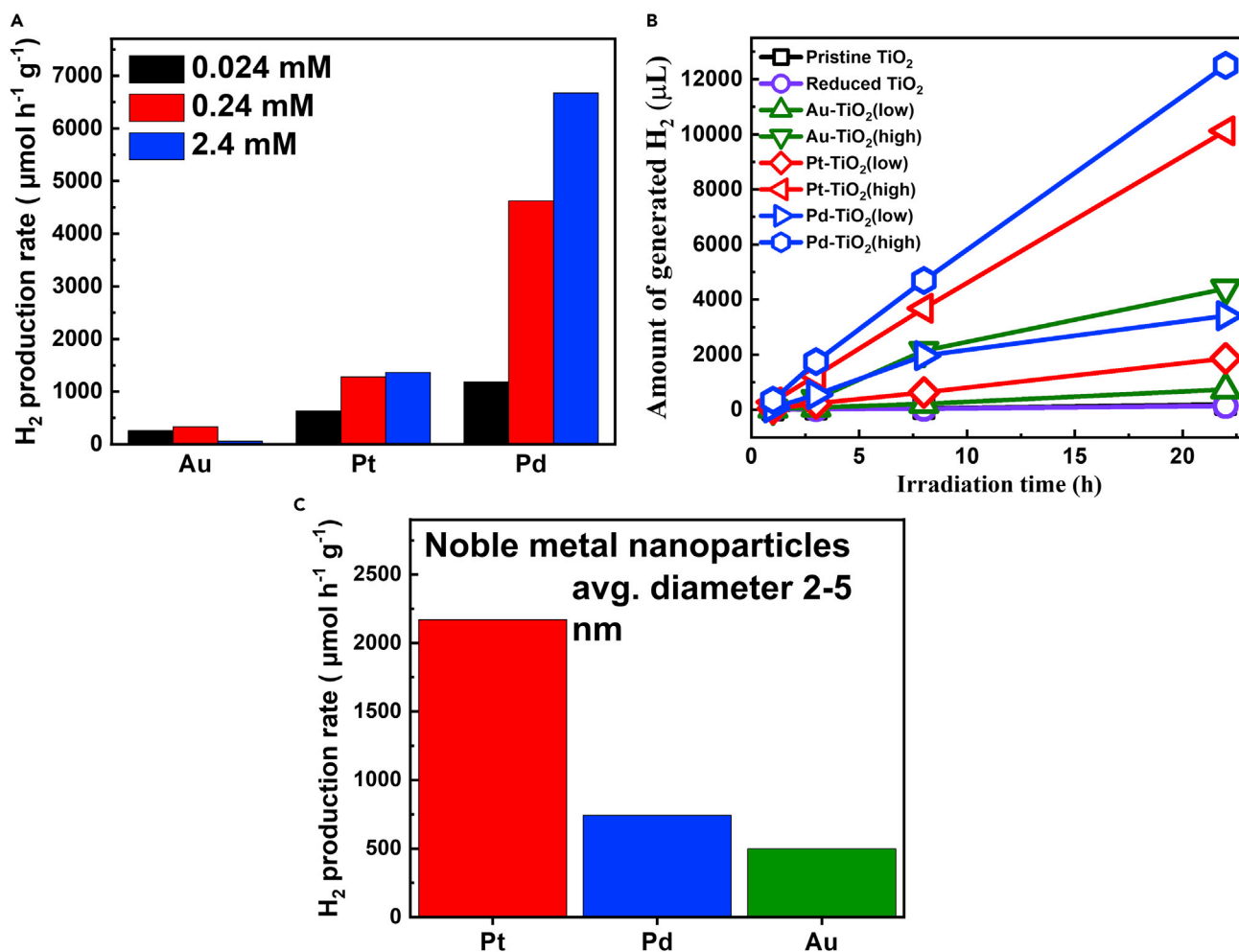
Figure 3. Photocatalytic H$_2$ evolution rate of noble metal-decorated TiO$_2$ nanosheets—SA (different concentration and longtime H$_2$ evolution) and nanoparticles

(A) Photocatalytic H$_2$ evolution rate for different concentrations of the precursor salts.

(B) Overview of the longtime H$_2$ evolution from TiO$_2$ nanosheets with different (low or high) noble metal SA loading (Au-TiO$_2$, Pt-TiO$_2$, and Pd-TiO$_2$).

(C) H$_2$ evolution rate of TiO$_2$ nanosheets decorated with noble metal nanoparticles with a diameter of $\approx$ 2–5 nm and loading of 1 wt. % (Pt, Pd, or Au, respectively) decorated nanoparticles.

reactive sites, the SA ones, to generate H$_2$. To model this process, we added one extra electron to the H@SA-TiO$_2$ and 2H@SA-TiO$_2$ models and observed that the charge localization is the most prominent for Pd SA. Hence, the conclusion is that effective photoelectrocatalysis by metal SA requires both appropriate H binding energetics and proper charge localization of photoelectrons by co-catalyst SA sites. Such physical background is depicted by the simple correlation between the photocatalytic activity (quantified by TOF) and the H adsorption energy multiplied by the extra charge localized on H in H@SA-TiO$_2$ and 2H@SA-TiO$_2$ systems (Figure 4), which confirms our hypothesis. These findings suggest that it is necessary to leave aside conventional volcano-type logic in SA catalysis and carefully reconsider the validity of activity descriptors established from bulk and nanomaterials. We believe that for the SA catalysts, one should look at each SA. Different behavior of Pd and Pt, on the one side, and Au SAs, on the other side, can also be seen when analyzing the electronic structures of the SAs embedded in the TiO$_2$ surface with hydrogen adatoms (Figure S9). Weak interaction of Au with the surface results in forming a molecule-like complex with hydrogen and weakened interaction with the TiO$_2$ surface. While this process is not expected for bulk and nanosized Au, we see it for Au SAs and link it to the activity losses visible in Figure 3. No such behavior arises during the simulations for Pd and especially Pt, which interacts the strongest with the TiO$_2$ surface.
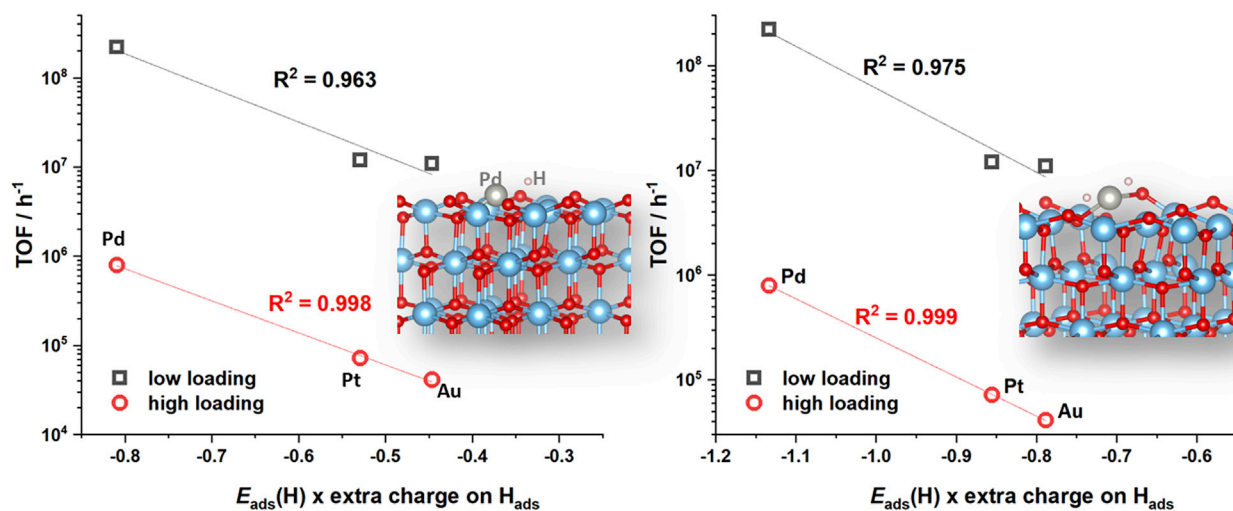
Figure 4. Straightening of the volcano for noble metal single atoms

Straightening of the volcano—the correlation of TOF and the adsorption energy of H on metal SAs multiplied by the extra charge on H_{ads} upon adding one electron to the system to simulate localization of mobile photoelectrons on metal SA sites. The case of one H_{ads} is given on the left, and the case of two H_{ads} is given on the right. Straight lines fit the data points while the determination coefficients are indicated.

Overall, the present work shows that as a single atom Pd can be significantly more effective as a cocatalyst for photocatalytic H_2 evolution than single atom Pt or Au. This deviation from the volcano paradigm is ascribed, based on DFT, to a different charge localization on the different noble metal SAs anchored in the TiO_2 surface.

STAR★METHODS

Detailed methods are provided in the online version of this paper and include the following:

- KEY RESOURCES TABLE
- RESOURCE AVAILABILITY
    - Lead contact
    - Materials availability
    - Data and code availability
- METHOD DETAILS
    - Synthesis of the TiO_2 nanosheets and their decoration with single atoms or nanoparticles
    - Characterization
    - Photocatalytic H_2 evolution measurements
    - Evaluation of the turnover frequency
    - Density functional theory calculations

SUPPLEMENTAL INFORMATION

Supplemental information can be found online at https://doi.org/10.1016/j.isci.2021.102938.

ACKNOWLEDGMENTS

REFERENCES

Daelman, N., Capdevila-Cortada, M., and López, N. (2019). Dynamic charge and oxidation state of Pt/CeO2 single-atom catalysts. Nat. Mater. *18*, 1215–1221. https://doi.org/10.1038/s41563-019-0444-y.

Flytzani-Stephanopoulos, M. (2014). Gold atoms stabilized on various supports catalyze the water-gas shift reaction. Acc. Chem. Res. *47*, 783–792. https://doi.org/10.1021/ar4001845.

Fu, Q., Saltsburg, H., and Flytzani-Stephanopoulos, M. (2003). Active nonmetallic Au and Pt species on ceria-based water-gas shift catalysts. Science *301*, 935–938. https://doi.org/10.1126/science.1085721.

Gao, C., Low, J., Long, R., Kong, T., Zhu, J., and Xiong, Y. (2020). Heterogeneous single-atom photocatalysts: fundamentals and applications. Chem. Rev. *120*, 12175–12216. https://doi.org/10.1021/acs.chemrev.9b00840.

Gates, B.C., Flytzani-Stephanopoulos, M., Dixon, D.A., and Katz, A. (2017). Atomically dispersed supported metal catalysts: perspectives and suggestions for future research. Catal. Sci. Technol. *7*, 4259–4275. https://doi.org/10.1039/c7cy00881c.

Giannozzi, P., Andreussi, O., Brumme, T., Bunau, O., Buongiorno Nardelli, M., Calandra, M., Car, R., Cavazzoni, C., Ceresoli, D., Cococcioni, M., et al. (2017). Advanced capabilities for materials modelling with Quantum ESPRESSO. J. Phys. Condens. Matter *29*, 465901. https://doi.org/10.1088/1361-648X/aa8f79.

Giannozzi, P., Baroni, S., Bonini, N., Calandra, M., Car, R., Cavazzoni, C., Ceresoli, D., Chiarotti, G.L., Cococcioni, M., Dabo, I., et al. (2009). Quantum ESPRESSO: a modular and open-source software project for quantum simulations of materials. J. Phys. Condens. Matter *21*, 395502. https://doi.org/10.1088/0953-8984/21/39/395502.

Giordano, L., Pacchioni, G., Bredow, T., and Sanz, J.F. (2001). Cu, Ag, and Au atoms adsorbed on TiO2(110): cluster and periodic calculations. Surf.

Sci. *471*, 21–31. https://doi.org/10.1016/S0039-6028(00)00879-7.

Heiz, U., Sanchez, A., Abbet, S., and Schneider, W.-D. (1999). Catalytic oxidation of carbon monoxide on monodispersed platinum clusters: each atom counts. J. Am. Chem. Soc. *121*, 3214–3217. https://doi.org/10.1021/ja983616l.

Hejazi, S., Mohajernia, S., Osuagwu, B., Zoppellaro, G., Andryskova, P., Tomanec, O., Kment, S., Zboril, R., and Schmuki, P. (2020). On the controlled loading of single platinum atoms as a Co-catalyst on TiO2 anatase for optimized photocatalytic H2 generation. Adv. Mater. *32*. 1908505 (1–9). https://doi.org/10.1002/adma.201908505.

Hu, Y., Qu, Y., Zhou, Y., Wang, Z., Wang, H., Yang, B., Yu, Z., and Wu, Y. (2021). Single Pt atom-anchored C3N4: a bridging Pt–N bond boosted electron transfer for highly efficient photocatalytic H2 generation. Chem. Eng. J. *412*, 128749. https://doi.org/10.1016/j.cej.2021.128749.

Kudo, A., and Miseki, Y. (2009). Heterogeneous photocatalyst materials for water splitting. Chem. Soc. Rev. *38*, 253–278. https://doi.org/10.1039/B800489G.

Lačnjevac, U., Vasilić, R., Dobrota, A., Đurđić, S., Tomanec, O., Zbořil, R., Mohajernia, S., Nguyen, N.T., Skorodumova, N., Manojlović, D., et al. (2020). High-performance hydrogen evolution electrocatalysis using proton-intercalated TiO2 nanotube arrays as interactive supports for Ir nanoparticles. J. Mater. Chem. A. *8*, 22773–22790. https://doi.org/10.1039/D0TA07492F.

Liu, J. (2017). Catalysis by supported single metal atoms. ACS Catal. *7*, 34–59. https://doi.org/10.1021/acscatal.6b01534.

Mohajernia, S., Andryskova, P., Zoppellaro, G., Hejazi, S., Kment, S., Zboril, R., Schmidt, J., and Schmuki, P. (2020). Influence of Ti3+ defect-type on heterogeneous photocatalytic H2 evolution activity of TiO2. J. Mater. Chem. A. *8*, 1432–1442. https://doi.org/10.1039/C9TA10855F.

Monkhorst, H.J., and Pack, J.D. (1976). Special points for Brillouin-zone integrations. Phys. Rev. B *13*, 5188–5192. https://doi.org/10.1103/PhysRevB.13.5188.

Naldoni, A., Altomare, M., Zoppellaro, G., Liu, N., Kment, Š., Zbořil, R., and Schmuki, P. (2019). Photocatalysis with reduced TiO2 : from black TiO2 to cocatalyst-free hydrogen production. ACS Catal. *9*, 345–364. https://doi.org/10.1021/acscatal.8b04068.

Nørskov, J.K., Bligaard, T., Logadottir, A., Kitchin, J.R., Chen, J.G., Pandelov, S., and Stimming, U. (2005). Trends in the exchange current for hydrogen evolution. J. Electrochem. Soc. *152*, J23. https://doi.org/10.1149/1.1856988.

Osterloh, F.E. (2013). Inorganic nanostructures for photoelectrochemical and photocatalytic water splitting. Chem. Soc. Rev. *42*, 2294–2320. https://doi.org/10.1039/C2CS35266D.

Parsons, R. (1958). The rate of electrolytic hydrogen evolution and the heat of adsorption of hydrogen. Trans. Faraday Soc. *54*, 1053. https://doi.org/10.1039/tf9585401053.

Perdew, J.P., Burke, K., and Ernzerhof, M. (1996). Generalized gradient approximation made simple. Phys. Rev. Lett. *77*, 3865–3868. https://doi.org/10.1103/PhysRevLett.77.3865.

Qiao, B., Wang, A., Yang, X., Allard, L.F., Jiang, Z., Cui, Y., Liu, J., Li, J., and Zhang, T. (2011). Single-atom catalysis of CO oxidation using Pt1/FeOx. Nat. Chem. *3*, 634–641. https://doi.org/10.1038/nchem.1095.

Seh, Z.W., Kibsgaard, J., Dickens, C.F., Chorkendorff, I., Nørskov, J.K., and Jaramillo, T.F. (2017). Combining theory and experiment in electrocatalysis: insights into materials design. Science *355*, eaad4998. https://doi.org/10.1126/science.aad4998.

Serpone, N., Salinaro, A., Emeline, A., and Ryabchuk, V. (2000). Turnovers and photocatalysis: a mathematical description.

J. Photochem. Photobiol. A. Chem. *130*, 83–94. https://doi.org/10.1016/S1010-6030(99)00217-8.

Sheng, W., Myint, M., Chen, J.G., and Yan, Y. (2013). Correlating the hydrogen evolution reaction activity in alkaline electrolytes with the hydrogen binding energy on monometallic surfaces. Energy Environ. Sci. *6*, 1509. https://doi.org/10.1039/c3ee00045a.

Trasatti, S. (1972). Work function, electronegativity, and electrochemical behaviour of metals. J. Electroanal. Chem. Interfacial Electrochem. *39*, 163–184. https://doi.org/10.1016/S0022-0728(72)80485-6.

Wang, A., Li, J., and Zhang, T. (2018). Heterogeneous single-atom catalysis. Nat. Rev. Chem. *2*, 65–81. https://doi.org/10.1038/s41570-018-0010-1.

Wang, Q., and Domen, K. (2020). Particulate photocatalysts for light-driven water splitting: mechanisms, challenges, and design strategies.

Chem. Rev. *120*, 919–985. https://doi.org/10.1021/acs.chemrev.9b00201.

Wang, Z., Yang, J., Gan, J., Chen, W., Zhou, F., Zhou, X., Yu, Z., Zhu, J., Duan, X., and Wu, Y. (2020). Electrochemical conversion of bulk platinum into platinum single-atom sites for the hydrogen evolution reaction. J. Mater. Chem. A. *8*, 10755–10760. https://doi.org/10.1039/D0TA02351E.

Wenderich, K., and Mul, G. (2016). Methods, mechanism, and applications of photodeposition in photocatalysis: a review. Chem. Rev. *116*, 14587–14619. https://doi.org/10.1021/acs.chemrev.6b00327.

Yang, X.-F., Wang, A., Qiao, B., Li, J., Liu, J., and Zhang, T. (2013). Single-atom catalysts: a new frontier in heterogeneous catalysis. Acc. Chem. Res. *46*, 1740–1748. https://doi.org/10.1021/ar300361m.

Yao, Y., Gu, X.-K., He, D., Li, Z., Liu, W., Xu, Q., Yao, T., Lin, Y., Wang, H.-J., Zhao, C.,

et al. (2019). Engineering the electronic structure of submonolayer Pt on intermetallic Pd 3 Pb via charge transfer boosts the hydrogen evolution reaction. J. Am. Chem. Soc. *141*, 19964–19968. https://doi.org/10.1021/jacs.9b09391.

Zhou, Z., Wang, S., Zhou, W., Wang, G., Jiang, L., Li, W., Song, S., Liu, J., Sun, G., and Xin, Q. (2003). Novel synthesis of highly active Pt/C cathode electrocatalyst for direct methanol fuel cell. Chem. Commun. *7*, 394–395. https://doi.org/10.1039/b211075j.

Zhu, C., Fu, S., Shi, Q., Du, D., and Lin, Y. (2017). Single-atom electrocatalysts. Angew. Chem. - Int. Ed. *56*, 13944–13960. https://doi.org/10.1002/anie.201703864.

Zubieta, C.E., Aquino-Linarez, L.G., Fuente, S.A., Belelli, P.G., and Ferullo, R.M. (2020). Growth and structure of Cu, Ag and Au clusters on α-Fe2O3(0001): a comparative density functional study. Comput. Mater. Sci. *173*, 109392. https://doi.org/10.1016/j.commatsci.2019.109392.

STAR★METHODS

KEY RESOURCES TABLE

REAGENT or RESOURCE	SOURCE	IDENTIFIER
Chemicals		
tetrabutyl titanate (Ti(OBu)$_4$)	Sigma-Aldrich Merck	CAS Number: 5593-70-4
hydrofluoric acid (HF, 48%)	Sigma-Aldrich Merck	CAS Number: 7664-39-3
(NH$_4$)$_2$PdCl$_6$	Sigma-Aldrich Merck	CAS Number: 19168-23-1
HAuCl$_4$×3H$_2$O	Sigma-Aldrich Merck	CAS Number: 16961-25-4
NaBH$_4$	Sigma-Aldrich Merck	CAS Number: 16940-66-2
NaOH	Sigma-Aldrich Merck	CAS Number: 1310-73-2
TiO$_2$ anatase nanoparticles	Sigma-Aldrich Merck	CAS Number: 1317-70-0
Software and algorithms		
Multipak software for XPS	Multipak - ULVAC-PHI	ULVAC-PHI, v9.3
Quantum ESPRESSO package	Quantum ESPRESSO Foundation (QEF)	v6.7

RESOURCE AVAILABILITY

Lead contact

Further information and requests for resources and reagents should be directed to and will be fulfilled by the lead contact, Prof. Patrik Schmuki (schmukiw@ww.uni-erlangen.de).

Materials availability

This study did not generate new unique reagents.

Data and code availability

No new data was reported from this study. This paper does not report original code. Any additional information required to reanalyze the data reported in this paper is available from the lead contact upon request.

METHOD DETAILS

Synthesis of the TiO$_2$ nanosheets and their decoration with single atoms or nanoparticles

Anatase nanosheets were synthesized by a hydrothermal method using commercially available reagents, tetrabutyl titanate (Ti(OBu)$_4$) and concentrated hydrofluoric acid (HF, 48%) from Sigma-Aldrich Merck. Both reagents were used as received without further purification. HF (1.2 mL) was added dropwise to Ti(OBu)$_4$ (10 mL) placed in a 250 mL Teflon liner, under stirring at room temperature. The stirring was continued for the next 40 min before the Teflon liner containing the mixture was sealed in an autoclave, which was eventually transferred to a preheated oven at 200°C. The reaction was completed after 24 h and the autoclave was allowed to cool in the oven. After the hydrothermal reaction, the precipitates were collected and washed with distilled water and ethanol several times and finally dried in an oven at 75°C overnight.

The resulting {001} TiO$_2$ nanosheets were then exposed to a reductive annealing in Ar/H$_2$ 10% at 200°C for 2 hours to produce Ti^{3+}-O$_v$ vacancies. Single atom decoration was then achieved by immediately

immersing the samples in H_2PtCl_6, $(NH_4)_2PdCl_6$, or $HAuCl_4 \times 3H_2O$ solutions. An identical loadings was adjusted using a series of XPS experiments from 0.1 mM to 10 mM of noble metal precursor salts in 100mL of distilled water.

Reference samples decorated with crystalline noble metal nanoparticles were prepared by using a modified polyol method (Zhou et al., 2003), using 1 wt. % of noble metal in the precursors (H_2PtCl_6, $(NH_4)_2PdCl_6$, and $HAuCl_4 \times 3H_2O$). For this TiO_2 nanosheets were dissolved in 20 mL ethylene glycol and ultrasonicated to form a homogeneous dispersion. The metal solutions were than added to the TiO_2 nanosheets dispersion and 30 mM $NaBH_4$ was slowly dropped into the mixtures. The solution was adjusted to pH 9 using 1 M NaOH (except for the Au solution), followed by heating for 30 min with vigorous stirring. Finally, the resulting products were separated in a centrifuge and dried in an oven overnight.

Characterization

The layers were investigated using a field emission scanning electron microscope (FE-SEM) Hitachi FE-SEM 4800. The chemical composition of the samples was analyzed by X-ray photoelectron spectroscopy (XPS, PHI 5600, US), and peak positions were shifted with respect to the C1s peak at 284.5 eV (Multipak software was used for fitting the peaks). X-ray diffraction analysis (XRD) was conducted with an X'pert Philips MPD (with a Panalytical X'celerator detector) using graphite monochromized Cu Kα radiation (λ = 1.54056 Å).

Transmission electron microscopy (TEM) was performed with a Titan[3] Themis 300, which is equipped with a high-brightness field-emission gun (X-FEG), a monochromator system (energy resolution 0.2 eV), two Cs-correctors (probe and image side) from CEOS (Corrected Electron Optical Systems GmbH), a Super-X detector (for energy dispersive X-ray spectroscopy), a Gatan Imaging Filter, a high-angle annular dark-field (HAADF) detector and a 4 k CMOS camera. This microscope was operated at 200 kV acceleration voltage.

A JEOL JES-X-320 EPR, equipped with a variable temperature control ES 13060DVT5 apparatus, was used for recording EPR spectra. Briefly the EPR spectra were all measured by using the following parameters: modulation frequency 100 kHz, modulation amplitude 0.5 mT, time constant 0.03 s, sweep time of 4 min and temperature T = 123 K. For additional details, see previously published work [27]. The EPR spectrum of commercial TiO_2 anatase nanoparticles (Sigma-Aldrich, 99.8%, 25–35 nm, BET $\approx$ 100 m^2/g) was also measured as reference.

The concentration level of the noble metal loading for high loading were also determined by atomic absorption spectroscopy (AAS) with electro thermal atomization (AAS-ETA) using a graphite furnace with a ContrAA 600 Spectrometer (Analytik Jena AG) equipped with a high-resolution Echelle double monochromator and with a continuum radiation source (Xe lamp).

IR-ATR measurements were performed using a Thermo Scientific Nicolet iS20 FTIR Spectrometer equipped with a diamond crystal. Data were recorded in the range from 400 to 4,000 cm^{-1}. All experiments were carried out at ambient conditions.

Photocatalytic H_2 evolution measurements

For the photocatalytic H_2 generation experiments the samples were immersed in a quartz tube containing 50 vol% methanol-water solution (photocatalytic reactor). It should be noted that methanol was used as a hole scavenger. The SA-decorated TiO_2 nanosheets samples (or the nanoparticle decorated TiO_2 nanosheets samples) were illuminated under 365 nm for 5 hr and up to 24 hr. The suspension was stirred at 1000 rpm. A chromatograph (GCMS-QO2010SE, SHIMADZU) with a TCD detector was used to measure the amount of generated H_2.

Evaluation of the turnover frequency

The turnover frequency (TOF) was determined from the generated H_2 flux and the density of single atoms. The turnover frequency (TOF) is generally defined as:

$$TOF = \frac{dmol(H)}{dt} \times \frac{1}{mol(A)}$$

where $dmol(H)/dt$ is the rate at hydrogen production per surface area, and $mol(A)$ is the number of moles of active catalyst sites per surface area.[1] In catalysis or especially in photocatalysis a number of different

approaches are considered to evaluate the number of active sites (Serpone et al., 2000). In our case the most straightforward approach is to directly determine the single atom density from HAADF-TEM images and consider the illumination area (≈ 1 cm^2 in our case) as the reactive area. Thus, the turnover frequencies (TOF) were calculated using the equation described below:

$$\text{TOF}\left(h^{-1}\right) = \frac{\text{number of evolved H}_2 \text{ molecules (per illuminated surface area)}}{\text{number of noble metal SA on TiO}_2 \text{(per illuminated surface area)} \times \text{reaction time}}$$

Please note that this definition deviates from other approaches used in photocatalysis (Serpone et al., 2000).

Density functional theory calculations

For DFT, to model the studied SA catalysts, we adopted the previously used approach (Lačnjevac et al., 2020) and considered SA metal trapping at the surface Ti^{3+}-O$_v$ sites of anatase TiO$_2$(001). Briefly, spin-un-restricted density functional theory (DFT) calculations, PBE-GGA approach (Perdew et al., 1996), were performed using the Quantum ESPRESSO package (Giannozzi et al, 2009, 2017). Ultrasoft pseudopotentials were employed with the plane-wave basis set expanded with a kinetic energy cutoff of 400 eV and a charge density cutoff 16 times higher. The sampling of the first irreducible Brillouin zone was done using the 2 × 2 × 1 Monkhorst–Pack k-point mesh (Monkhorst and Pack, 1976). Using the 3 × 3 unit cell of anatase TiO$_2$(001), the concentration of SAs was 1.04 at.%. Metal SAs were embedded into the surface Ov site, and the electronic structures and H binding were investigated. All the atoms in the cell were fully relaxed, except the two bottom layers of the slab. To quantify the interactions of metal SAs with the O-deficient TiO$_2$ surface or the interaction of hydrogen with embedded metal SAs, we used the adsorption energy generally defined as:

$$E_{ads}(X) = (E_{surface} + X - E_{surface} - nE_X)/n$$

where $E_{surface+X}$ stands for the total energy of the surface with adsorbate, $E_{surface}$ is the total energy of the surface without adsorbate X, while E_X is the total energy of isolated adsorbate X. Number of adsorbates is defined by n.